Programming characteristics of electrochemical random-access memory (ECRAM) - Part I: Experimental Study

M. Porzani, *Graduate Student Member, IEEE*, S. Ricci, M. Farronato, *Member, IEEE*, D. Ielmini, *Fellow, IEEE*

***Abstract*—Electrochemical random-access memory (ECRAM) based on transition metal oxides is a promising candidate as a next generation synaptic device for in-memory computing, due to its highly-linear weight update characteristic and compatibility with the CMOS process. Understanding the conductance modulation mechanisms is essential to better improve device performance, reliability and scalability. This work addresses the programming characteristics of ECRAM devices with WO_x channel and Ta_2O_5 electrolyte. Large conductance modulation is achieved under quasi-static transcharacteristic measurements and interpreted with a nonlinear ionic drift-diffusion mechanism for oxygen vacancy migration. The linear conductance update is characterized as a function of pulse voltage amplitude and time duration, and the limits of the small signal approximation are discussed and experimentally assessed.**

***Index Terms*—ECRAM, emerging memory technologies, in-memory computing, neuromorphic computing, synaptic weight.**

I. Introduction

In-memory computing (IMC) is a new computing paradigm, where memory and processing units are merged in a single entity in which both data processing and storage are co-located on the same physical area on the chip [1]–[3]. To implement IMC, resistive memory devices have attracted high interest thanks to their analog non-volatile storage of weight, linear and symmetric weight update characteristics, and fast programming operations [4]. Two-terminal (2-T) non-volatile memory devices such as resistive-switching random-access memory (RRAM) [5] and phase change memory (PCM) [6] have so far been successfully implemented in IMC architectures [7] [8] [9]. The conductance G of these devices is strongly dictated by nanometer-sized regions, like conducting filaments for RRAMs, where the atomic nature of these switching processes poses a number of issues such as stochasticity, read-out noise and non-ideal synaptic behavior. Three-terminal (3-T) devices have been proposed as an alternative synaptic element to overcome these limitations, by introducing a third terminal to control conductance modulation, at the price of a more complicated elementary cell [10]. Among the 3-T devices, the electrochemical random-access memory (ECRAM) [11]–[13] is a 3-T resistive memory device, where analog information is stored in a conducting channel, and switched by ion injection across an electrolyte barrier. Its structure allows to effectively decouple read and write paths to suppress program disturb and support linear programming characteristics. Li-based ECRAM were first proposed due to higher mobility of the small lithium ion [14], although open-circuit potentials and poor compatibility with the CMOS process create significant

Submitted for review on 18/12/2023. This work received funding from ECSEL Joint Undertaking (JU) under grant agreement no. 101007321. The JU receives support from the European Union's Horizon 2020 research and innovation programme and France, Belgium, Czech Republic, Germany, Italy, Sweden, Switzerland, Turkey.

M. Porzani, S. Ricci, M. Farronato and D. Ielmini are with the Dipartimento di Elettronica, Informazione e Bioingegneria, Politecnico di Milano, 20133 Milan, Italy (e-mail: daniele.ielmini@polimi.it).

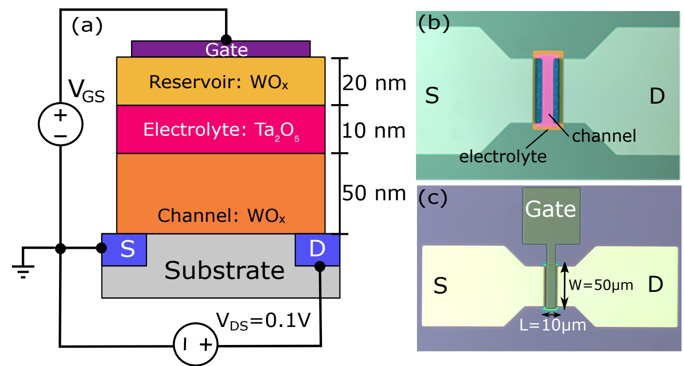

Fig. 1. ECRAM structure. (a) Schematic illustration of the cross-section and bias scheme. (b) Top-view optical micrograph after the deposition of the reservoir layer. (c) Top-view micrograph after the deposition of the gate electrode.

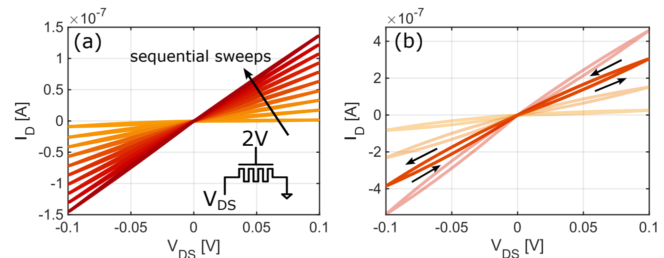

Fig. 2. ***I*-*V*** characteristic for an ECRAM device at constant gate polarization V_{GS} = 2 V. (a) Drain current for ten sequential voltage sweeps, with an increase of channel conductance with time. (b) Highlight of a single voltage sweep where a counterclockwise hysteresis can be observed.

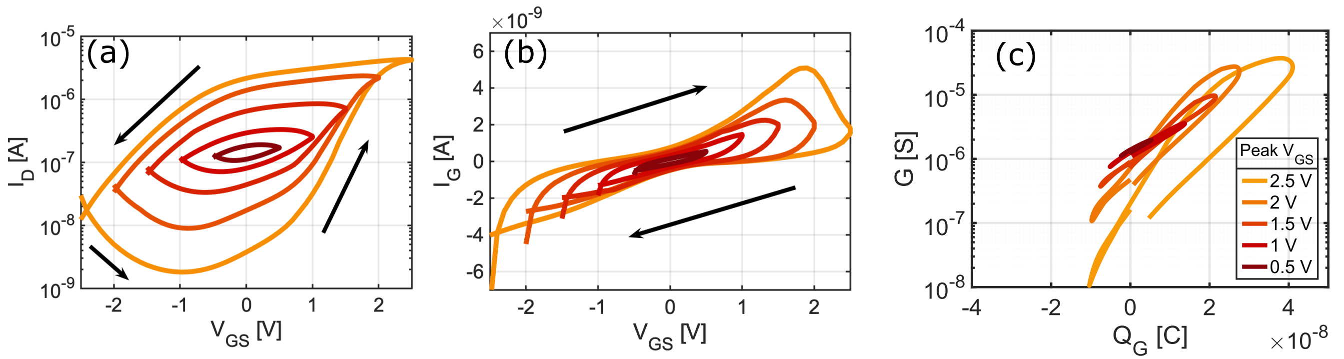

Fig. 3. Quasi-static characterization of the ECRAM. (a) Channel current I_D and (b) gate current I_G transcharacteristic curves obtained by applying gate voltage ramps at different voltage amplitude and 60 s ramp time. (c) Relation between channel conductance G, obtained with Ohm's law, and the total charge injected in the gate terminal, obtained by integrating I_G as shown in Eq. (1).

challenge. Most recently, metal oxide-based ECRAM [11] were introduced where oxygen vacancies (V_o) serve as mobile species for channel ion intercalation to achieve conductance modulation. Despite some preliminary modeling analysis [15], the details of the electrical device characteristics and the origins/limitations of the linear programming operation are not fully clarified to date. This paper presents a comprehensive study of the ECRAM experimental electrical characterization, from the standpoint of both large quasi-static channel conductance modulation and linear pulsed conductance update. The results are discussed and interpreted on the basis of a drift-diffusion process for oxygen vacancies. Based on this experimental study and mechanism understanding, a physical, numerical and analytical model will be presented in the companion paper [16].

II. Experimental Devices and Setup

Fig. 1(a) shows the sketch of a vertical cross-section of the ECRAM devices fabricated for this analysis. Source and drain platinum (Pt) electrodes were deposited via e-beam evaporation on an insulating silicon oxide (SiO_2) substrate over a silicon wafer. The channel is a 50 nm thick tungsten oxide (WO_x) film obtained with reactive sputtering deposition in a low oxygen plasma with Ar:O_2 flux ratio of 30:3 standard cubic centimetres per minute (SCCM) injected in the chamber at 50 W power, and then annealed in vacuum at 400° C for 15 minutes. The annealing step allowed to reach the stoichiometric-oxide composition and relatively low resistivity for device operation. A 10 nm Ta_2O_5 electrolyte layer and a 20 nm WO_x reservoir layer are then deposited on top of the channel by e-beam evaporation. The oxide layers fully cover the channel as shown in Fig. 1(b), to serve as a capping protective layer. A Ti/TiN gate is finally deposited by e-beam evaporation on top of the cell, as shown in Fig. 1(c). All patterning steps are performed by optical lithography techniques. All measurements were carried out on devices with area $W \times L = 50\,\mu m \times 10\,\mu m$. Quasi-static electrical measurement were performed with an Agilent 4156C Semiconductor Parameter Analyzer, while pulsed experiments were carried out with a Keithley 4200A Parameter Analyzer.

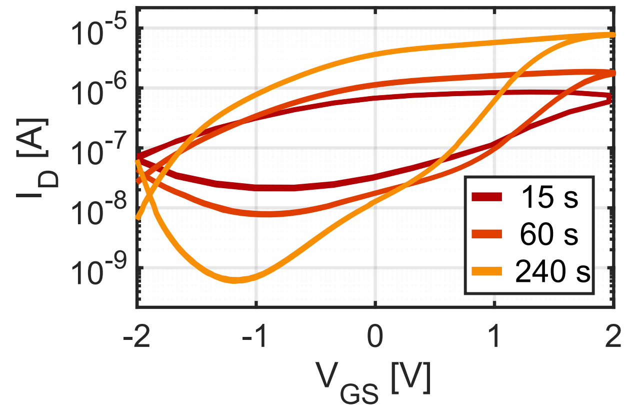

Fig. 4. Channel current I_D transcharacteristic curve measured as a function of ramp time. Hysteresis area and on-off ratio increase with ramp time.

III. Quasi-static characterization

Fig. 2(a) shows ten consecutive I-V characteristics of an ECRAM device, with a constant gate bias $V_{GS} = +2\,V$ and alternated bipolar sweep of the drain-source voltage V_{DS}. The positive V_{GS} induces an electric field inside the electrolyte layer that activates V_o injection from the reservoir to the channel [17]. The slope of the channel current, namely the conductance G, increases with each cycle as a result of the increase in V_o concentration. In this case a constant V_o injection rate would result in a continuous conductance increase with time. Fig. 2(b) highlights the I-V curve measured for a single sweep indicating a counterclockwise hysteresis under both polarities. Note that we can neglect the electric field across the channel length $\approx 0.1\,V/10\,\mu m$, which is much lower than the vertical field $\approx 1\,V/10\,nm$ in the experiment of Fig. 2.

A. Gate transcharacteristic

To provide a more systematic analysis of the channel conductance as a function of V_{GS}, we performed transcharacteristic measurements, consisting in the application of a voltage triangular ramp at the gate, while a constant $V_{DS} = 0.1\,V$ was maintained to monitor the drain current. Fig. 3 shows (a)

drain current I_D and (b) gate current I_G as a function of the gate voltage V_{GS}. Several transcharacteristic measurements are shown, with peak V_{GS} ranging from ±0.5 to $\pm2.5\,V$. Total measurement time was kept constant to 60 s. The current I_D describes a counterclockwise hysteresis loop, where the hysteresis area increases with peak V_{GS} amplitude, as the higher electric fields allow stronger ion injection/extraction. I_G can be attributed to the ionic current related to V_o migration [17], with a negligible electronic leakage contribution. The measured ion current scales with V_{GS} amplitude with a clockwise hysteresis as shown in Fig. 3(b).

These results can be interpreted with a field-induced ionic drift-diffusion mechanism for V_o migration [15], [18]–[20], where oxygen vacancies can both diffuse isotropically following concentration gradient and migrate under the effect of an external electric field. I_D and I_G are closely related, since a large I_G indicates a large V_o injection into the channel, leading to a steep increase of channel conductance G. The large swings in channel G are attributed to the migration of a large quantity of V_o from the reservoir to the channel and *viceversa*.

Fig. 3(c) shows measured G as a function of the computed injected charge Q_G, given by:

$$Q_G(t) = \int_0^t I_G(t)dt, \tag{1}$$

that, if electronic leakage is neglected, can be used to approximate the total amount of V_o injected in the channel volume. All measurements almost overlap, suggesting that the plot refers to a channel material property independent to applied V_{GS}. The curve spans several orders of magnitude in conductance modulation for a linear total charge injection, thus suggesting a highly non-linear dependence between the total oxygen vacancy concentration in tungsten oxide and its electrical conductivity [21]–[23].

Fig. 4 shows I_D hysteresis for increasing ramp time, for a given maximum V_{GS} peak. Hysteresis area increases with increasing ramp time, with both higher peak current and lower depression current, thus resulting in an increased on/off ratio. This behavior is expected from a drift-diffusion interpretation of V_o migration in the device. Indeed, the balance between diffusion and drift-induced V_o injection that gives the characteristic hysteresis shape is strongly dependent on the time duration of the applied electric fields.

B. PUND transcharacteristic

Fig. 5 shows (a) channel current I_D and (b) gate current I_G for a Positive Up, Negative Down (PUND) measurement [24] [25] consisting of two positive triangular half-waves followed by two negative triangular half-waves applied at the gate (see inset of Fig. 5a). All half-waves are $30\,s$ long and five consecutive cycles are shown. The first positive half-wave features a low-to-high I_D transition on the rising ramp, corresponding to a significant I_G peak due to V_o injection. The falling ramp presents a slightly decreasing current level, as the electric fields decrease with decreasing V_{GS}, thus resulting in some back-diffusion and consequent decrease of V_o concentration. The second positive half-wave does not significantly change the conductive state of the device, since the channel V_o concentration is already relatively large. I_G is correspondingly much lower in ramp #2 compared to ramp #1, since there is little ion migration to contribute to the measured current. Ramp #3 with negative V_{GS} results in a significant drop of conductance, or depression, due to large extraction of V_o from the channel, while ramp #4 only partially depresses an already V_o-depleted channel. Once again, a high conductance depression is linked with a relatively large gate current observed in Fig. 5(b).

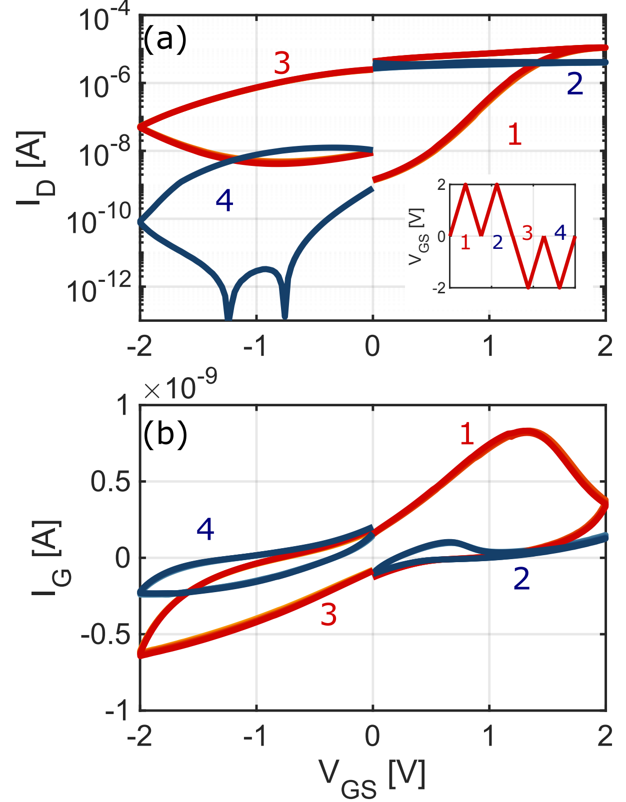

Fig. 5. Positive Up, Negative Down (PUND) quasi-static characteristic consisting of two positive voltage ramps followed by two negative voltage ramps as displayed in the inset of (a). Measured (a) $\boldsymbol{I_D}$ and (b) $\boldsymbol{I_G}$ for a 2 V gate peak, 60 s ramp time.

It is also interesting to notice that the measurements of the first positive and first negative waves (ramp #1 and #3 in Fig. 5), that are associated with the largest extractions of V_o defects, display the same behavior of a standard transcharacteristic as in Fig. 3. This can be attributed to the migration of V_o between channel and reservoir, that gives rise to the large hysteresis.

C. Role of the reservoir

To study the role of the reservoir layer in the quasi-static characteristic of the ECRAM, we conducted experiments on ECRAM devices without the reservoir layer as shown in the schematic cross-section structure in Fig. 6(a). The devices were fabricated on a companion chip to the main ECRAM chip measured in this paper. All fabrication steps were identical and performed in the same deposition session, to minimize

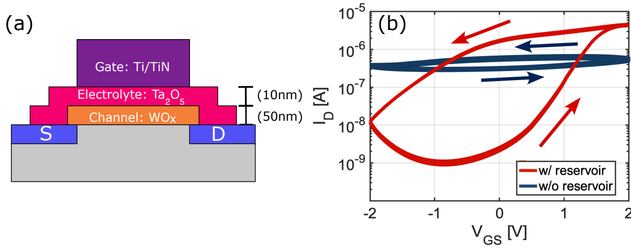

Fig. 6. Characterization of an ECRAM without reservoir. (a) Schematic illustration of the cross-section of an ECRAM without reservoir layer. (b) Comparison between the drain current hysteresis curve for ECRAM and ECRAM without reservoir measured at 2 V peak and 60 s ramp time.

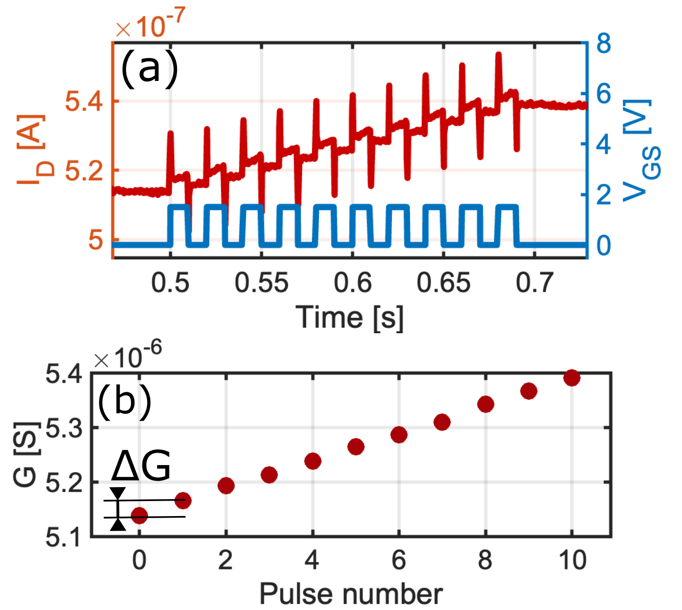

Fig. 7. Pulsed experiment characterization of ECRAM. (a) Measured channel current $\boldsymbol{I_D}$ for a train of ten programming gate pulses with $\boldsymbol{V_{GS}}$ = 1.5 V, $\boldsymbol{t_p}$ = 10 ms and 10 ms between each pulse. (b) Measured channel $\boldsymbol{G}$ as a function of applied gate pulse, with discrete $\boldsymbol{\Delta G}$ steps.

chip-to-chip variability. Fig. 6(b) shows a comparison between hysteresis transcharacteristics for an ECRAM and its counterpart without the reservoir layer. The I_D hysteresis is strongly reduced in the device without reservoir layer. This behavior can be explained by a lack of V_o to be supplied to the channel during positive voltage injection and the lack of a physical layer to store extracted V_o on negative voltage ramp, thus resulting in a significantly narrower current window. The small residual hysteresis can be attributed to the V_o exchange between the channel and the thin electrolyte layer [26].

IV. Pulsed Experiment Characterization

ECRAM application in IMC is crucial because of its linear weight-update characteristic [13], [27]. The application of a positive voltage pulse at the gate causes the injection of just a modest quantity of oxygen vacancies in the channel, increasing its conductance by a ΔG amount. Analogously, channel depression can be achieved with negative pulses.

Fig. 7(a) shows I_D measured during the application of a train of ten pulses, with $V_{GS} = 1.5$ V, $t_p = 10$ ms and 10 ms pause between each pulse. I_D increases during each V_{GS} pulse application, while it remains approximately constant during the read phase at $V_{GS} = 0$ V, that is performed with the application of a small $V_{DS} = 0.1$ V to avoid any disturbance to the conductance state of the channel. Fig. 7(b) shows the measured G after each pulse, indicating a linear increase with ten discrete ΔG steps, where the increment ΔG is a constant. The relatively small G window shown in Fig. 7 is a byproduct of a programming operation with constant V_{GS} and short t_p. By applying pulses with increasing amplitude, longer pulses and larger number of pulses, one can achieve a larger on-off ratio, similar to the quasi-static hysteresis in Fig. 4, where the much longer time scales coupled with an increasing V_{GS} ramp allow large G modulation.

Fig. 8 shows (a) $I_D - I_{D,ref}$ and (b) $G - G_{ref}$ as a function of V_{GS}, where $I_{D,ref}$ and G_{ref} are respectively drain current and channel conductance reference values measured at the beginning of the experiment. The slope increases with absolute voltage amplitude, as the higher electric fields increase V_o injection/extraction in the channel, hence the amplitude of the modulation. A slight asymmetry between potentiation and depression is seen. To highlight the features of pulsed programming we focus on the positive V_{GS} polarity. Fig. 9 shows median ΔG extracted from multiple pulsed potentiation experiments, varying both amplitude and t_p duration. Data can be described by the formula:

$$\Delta G = A t_p \exp\left(\alpha \frac{qV}{k_B T}\right) \tag{2}$$

where $A = 1.40 \times 10^{-7}\, S/s$ and $\alpha = 0.046$ are fitting constants extracted from the data, q, k_B and $T = 300\, K$ are respectively the electron charge, the Boltzmann constant and the device temperature. Fig. 9 shows that the ECRAM can be precisely programmed with conductance increase proportional to the time duration of the pulse and exponentially increasing with V_{GS}. Theoretical studies on drifting of ions in solid matter indicate that the migration rate in oxides depends exponentially on the voltage as it activates ion-hopping in the direction of the electric field [18], [19], [28]. Note the wide range of programmability which makes the ECRAM an excellent candidate for future applications in IMC. Eq. (2) provides an accurate approximation of ΔG in the medium V_{GS} range and short t_p regime, which can be used to model a wide range of conductance modulation. However, at low and high V_{GS}, and at relatively long programming times, data shows a deviation from the trend of Eq. (2), which raises the need for a more accurate description of device operation. This can be explained by the linearization of the V_{GS} dependence at low fields and the non-linear dependence of conductance on V_o concentration, as discussed in the companion paper [16].

A. Saturation and non-linear behavior

Since a linear ΔG is a desirable synaptic characteristic for ECRAM devices in IMC applications [29] [30], it is important to characterize the limits of the linear model of Eq. (2). In an IMC architecture to accelerate training of neural networks, the weights are stored directly in memory arrays

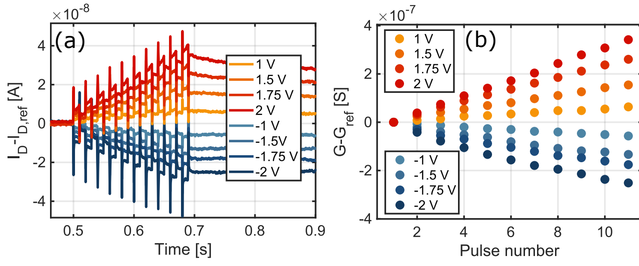

Fig. 8. Pulsed experiment characterization of ECRAM as a function of pulse amplitude for ten gate pulses with t_p = 10 ms and 10 ms pause between each pulse. (a) Measured $I_D - I_{D,ref}$. (b) Measured channel $G - G_{ref}$ after each pulse. $I_{D,ref}$ and G_{ref} are reference values measured at the start of the experiment.

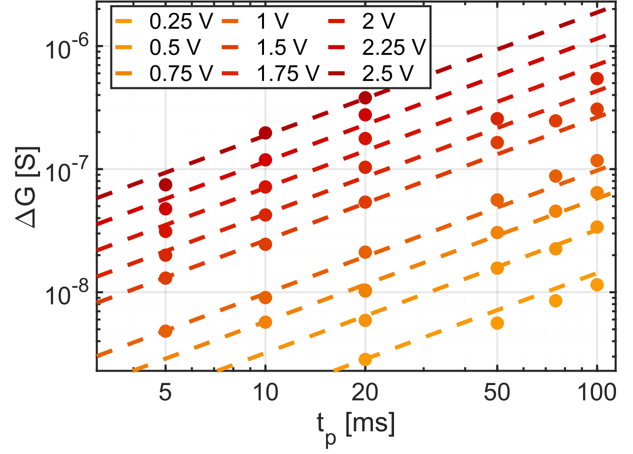

Fig. 9. Characterization of ECRAM pulse programming. Median experimental value of ΔG as a function of V_{GS} pulse amplitude and t_p duration, and linear fitting of the data as described by Eq. (2).

(for example in the channel G of ECRAM), and are updated with each training cycle [31]. The accuracy of the neural network is directly related to the programming precision of the devices, thus the need for reproducible analog programming in all devices. In particular, an ideal ECRAM described by Eq. (2) refers to a linear dependence on gate voltage pulse duration t_p or number of voltage pulses, that allows for controlled channel ΔG update and enables implementation in IMC structures. Two main non-idealities can be identified in the experimental characterization of single pulse ECRAM programming, namely (i) saturation and (ii) non-linearity. Fig. 10(a) shows saturation in the I_D characteristics as a function of programming time for a $V_{GS} = 2$ V, and $t_p = 100$ ms. Current saturation can be explained by large amount of V_o in the channel, causing back-diffusion towards the reservoir, thus counter-balancing the field-induced injection. After pulse potentiation a decay of the current due to diffusion mechanisms is observed. The conductance state in our ECRAM devices is thus semi-nonvolatile, with relevant analogy to the mechanism of short-term memory in biological synapses [32]. Saturation is more easily observed at high pulse voltage amplitudes and/or long programming times, which cause a relatively high V_o concentration in the channel. Fig. 10(b) shows the measured I_D and I_G for $V_{GS} = 1$ V and $V_{DS} = 0.1$ V as a function of time. I_D increases with a sharp slope followed by current saturation in about 15 s of voltage application. The current level reached with $1V$ application is similar to the peak reached for a $\pm 1V$ transcharacteristic in Fig. 3, suggesting that the device has reached a steady-state regime with a balance between drift injection and back-diffusion. I_G time evolution is a superposition of a large ionic current spike at the beginning, corresponding to the channel potentiation, and a slow decaying transient where electronic leakage could be relevant. The very low leakage of few pA can be attributed to the series resistance of the highly resistive electrolyte layer.

A second non-ideality is the non-linearity. This can be explained by the non-linear relationship between defect concentration and conductance in Fig. 3(c). For relatively large changes of V_o, the conductance increase displays a non-linear behavior, followed by saturation at even higher concentrations. To summarize the effects of these non-idealities, Fig. 11 shows ΔG as a function of the pulse number obtained by applying ten pulses with $t_p = 20$ ms at different voltage amplitudes.

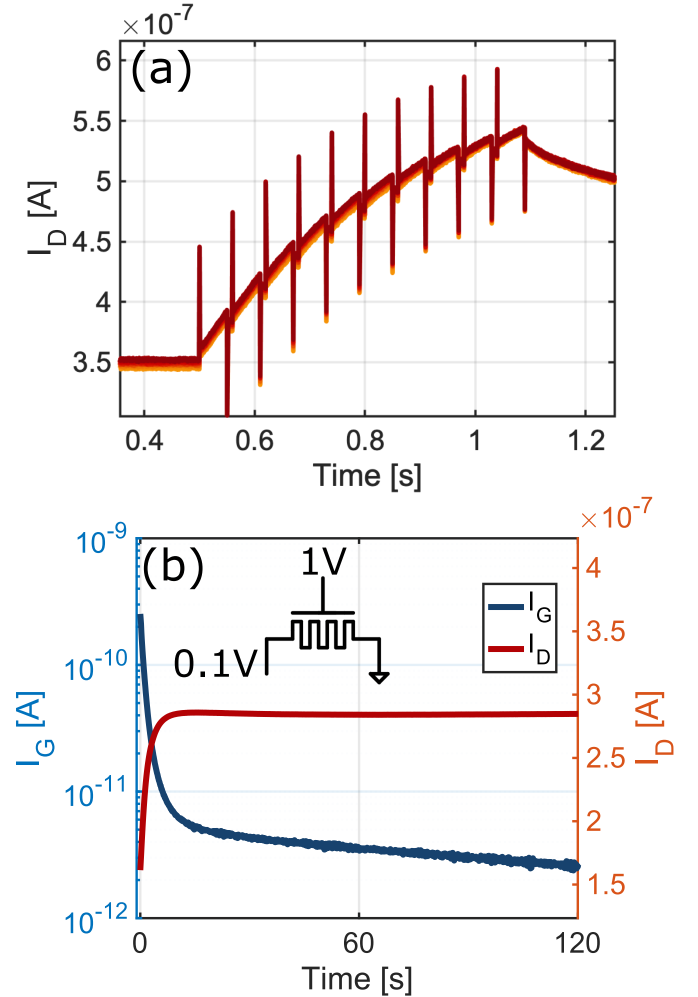

Fig. 10. Saturation behavior of the ECRAM. (a) Measured I_D for a 2 V amplitude, 100 ms duration sequence of programming pulses. (b) measured I_D and I_G for a 120 s constant 1 V gate voltage application.

A constant ΔG with time implies a constant increase in conductance with each pulse, hence a linear potentiation

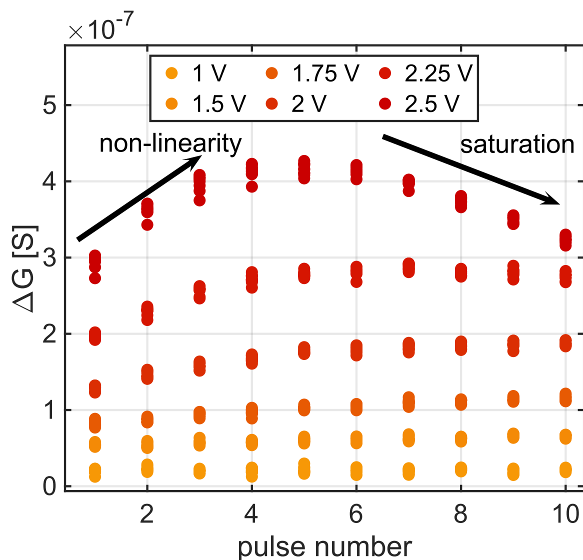

Fig. 11. **ΔG** measured as a function of the pulse number for trains of 20 ms pulses at various voltage amplitudes. It can be appreciated how for low voltage amplitude, **ΔG** is uniform with pulse time, while non-ideality deviations become nonnegligible at high voltage amplitudes.

characteristic, as observed for relatively low V_{GS}. At higher voltages non-idealities become relevant due to the relatively high V_o injection. At first the non-linearity leads to a positive increment in ΔG, followed by a decrease of ΔG due to the saturation effects. These phenomena have to be considered for the design of IMC circuits based on ECRAM.

V. Conclusions

We presented an experimental study of oxygen-based ECRAM devices, focusing both on large signal characteristics and small signal conductance modulation. We have shown that quasi-static I-V characteristics display a large hysteresis, and further investigated the role of the reservoir layer and the behavior under PUND measurements. We qualitatively linked the gate current hysteresis to the ionic injection in the channel and its conductance modulation. We presented pulsed programming characteristics with a large range of operation, and discussed saturation and non-linearity effects which characterize the strong-injection regime. These results provide a comprehensive framework for the understanding and the modeling of ECRAM devices for IMC applications.

VI. Acknowledgements

The authors would like to thank C. Somaschini, M. Asa, A. Scaccabarozzi, C. Nava, E. Sogne and S. Bigoni for the help in the fabrication process. This work was partially performed in Polifab, the micro- and nanofabrication facility of Politecnico di Milano.

References

[1] D. Ielmini *et al.*, "In-memory computing with resistive switching devices," *Nat Electron*, vol. 1, no. 6, pp. 333–343, Jun. 2018. doi: 10.1038/s41928-018-0092-2

[2] ——, "Emerging neuromorphic devices," *Nanotechnology*, vol. 31, no. 9, p. 092001, Feb. 2020. doi: 10.1088/1361-6528/ab554b

[3] P. Mannocci *et al.*, "In-memory computing with emerging memory devices: Status and outlook," *APL Machine Learning*, vol. 1, no. 1, p. 010902, Mar. 2023. doi: 10.1063/5.0136403

[4] D. Ielmini *et al.*, "Device and Circuit Architectures for In-Memory Computing," *Advanced Intelligent Systems*, vol. 2, no. 7, p. 2000040, Jul. 2020. doi: 10.1002/aisy.202000040

[5] F. Nardi *et al.*, "Resistive Switching by Voltage-Driven Ion Migration in Bipolar RRAM—Part I: Experimental Study," *IEEE Trans. Electron Devices*, vol. 59, no. 9, pp. 2461–2467, Sep. 2012. doi: 10.1109/TED.2012.2202319

[6] S. Ambrogio *et al.*, "Equivalent-accuracy accelerated neural-network training using analogue memory," *Nature*, vol. 558, no. 7708, pp. 60–67, Jun. 2018. doi: 10.1038/s41586-018-0180-5

[7] P. Mannocci *et al.*, "A Generalized Block-Matrix Circuit for Closed-Loop Analog In-Memory Computing," *IEEE J. Explor. Solid-State Comput. Devices Circuits*, vol. 9, no. 1, pp. 47–55, Jun. 2023. doi: 10.1109/JXCDC.2023.3265803

[8] S. Ricci *et al.*, "Forming-Free Resistive Switching Memory Crosspoint Arrays for In-Memory Machine Learning," *Advanced Intelligent Systems*, vol. 4, no. 8, p. 2200053, Aug. 2022. doi: 10.1002/aisy.202200053

[9] Z. Sun *et al.*, "Solving matrix equations in one step with cross-point resistive arrays," *Proc. Natl. Acad. Sci. U.S.A.*, vol. 116, no. 10, pp. 4123–4128, Mar. 2019. doi: 10.1073/pnas.1815682116

[10] M. Farronato *et al.*, "Reservoir Computing with Charge-Trap Memory Based on a MoS_2 Channel for Neuromorphic Engineering," *Advanced Materials*, vol. 35, no. 37, p. 2205381, Sep. 2023. doi: 10.1002/adma.202205381

[11] S. Kim *et al.*, "Metal-oxide based, CMOS-compatible ECRAM for Deep Learning Accelerator," in *2019 IEEE International Electron Devices Meeting (IEDM)*. San Francisco, CA, USA: IEEE, Dec. 2019, pp. 35.7.1–35.7.4. doi: 10.1109/IEDM19573.2019.8993463

[12] P. M. Solomon *et al.*, "Transient Investigation of Metal-oxide based, CMOS-compatible ECRAM," in *2021 IEEE International Reliability Physics Symposium (IRPS)*. Monterey, CA, USA: IEEE, Mar. 2021, pp. 1–7. doi: 10.1109/IRPS46558.2021.9405156

[13] H. Kang *et al.*, "Ion-Driven Electrochemical Random-Access Memory-Based Synaptic Devices for Neuromorphic Computing Systems: A Mini-Review," *Micromachines*, vol. 13, no. 3, p. 453, Mar. 2022. doi: 10.3390/mi13030453

[14] J. Tang *et al.*, "ECRAM as Scalable Synaptic Cell for High-Speed, Low-Power Neuromorphic Computing," in *2018 IEEE International Electron Devices Meeting (IEDM)*. San Francisco, CA: IEEE, Dec. 2018, pp. 13.1.1–13.1.4. doi: 10.1109/IEDM.2018.8614551

[15] M. Baldo *et al.*, "Modeling of oxide-based ECRAM programming by drift-diffusion ion transport," in *2021 IEEE International Memory Workshop (IMW)*. Dresden, Germany: IEEE, May 2021, pp. 1–4. doi: 10.1109/IMW51353.2021.9439608

[16] M. Porzani, "Programming characteristics of electrochemical random-access memory (ECRAM) - Part II: Physics-based Modeling," *IEEE Trans. Electron Devices*, 2023.

[17] Y. Jeong *et al.*, "Elucidating Ionic Programming Dynamics of Metal-Oxide Electrochemical Memory for Neuromorphic Computing," *Adv Elect Materials*, vol. 7, no. 8, p. 2100185, Aug. 2021. doi: 10.1002/aelm.202100185

[18] D. Ielmini *et al.*, "Analytical model for subthreshold conduction and threshold switching in chalcogenide-based memory devices," *Journal of Applied Physics*, vol. 102, no. 5, p. 054517, Sep. 2007. doi: 10.1063/1.2773688

[19] N. F. Mott *et al.*, *Electronic processes in ionic crystals*, 2nd ed. New York: Dover, 1964, oCLC: 229912023.

[20] S. Larentis *et al.*, "Resistive Switching by Voltage-Driven Ion Migration in Bipolar RRAM—Part II: Modeling," *IEEE Trans. Electron Devices*, vol. 59, no. 9, pp. 2468–2475, Sep. 2012. doi: 10.1109/TED.2012.2202320

[21] J. Lee *et al.*, "Improved Synaptic Characteristics of Oxide-Based Electrochemical Random Access Memory at Elevated Temperatures Using Integrated Micro-Heater," *IEEE Trans. Electron Devices*, vol. 69, no. 4, pp. 2218–2221, Apr. 2022. doi: 10.1109/TED.2022.3151306

[22] X. Zheng, "The influence of ion implantation-induced oxygen vacancy on electrical conductivity of WO3 thin films," *Vacuum*, vol. 165, pp. 46–50, Jul. 2019. doi: 10.1016/j.vacuum.2019.04.004

[23] J. Lee *et al.*, "Excellent synaptic behavior of lithium-based nano-ionic transistor based on optimal $WO_{2.7}$ stoichiometry with high ion diffusivity," *Nanotechnology*, vol. 31, no. 23, p. 235203, Mar. 2020. doi: 10.1088/1361-6528/ab793d

[24] H.-K. Peng *et al.*, "Enabling large memory window and high reliability for FeFET memory by integrating AlON interfacial layer,"

Applied Physics Letters, vol. 118, no. 10, p. 103503, Mar. 2021. doi: 10.1063/5.0036824
[25] J. Müller *et al.*, “Ferroelectric Zr0.5Hf0.5O2 thin films for nonvolatile memory applications,” *Applied Physics Letters*, vol. 99, no. 11, p. 112901, Sep. 2011. doi: 10.1063/1.3636417
[26] H. Kim *et al.*, “Impact of Oxygen Reservoir Layer on 3T Oxygen Ion-based Electrochemical Random Access Memory Performance,” *Adv Elect Materials*, vol. 9, no. 7, p. 2300133, Jul. 2023. doi: 10.1002/aelm.202300133
[27] A. A. Talin *et al.*, “ECRAM Materials, Devices, Circuits and Architectures: A Perspective,” *Advanced Materials*, vol. 35, no. 37, p. 2204771, Sep. 2023. doi: 10.1002/adma.202204771
[28] D. B. Strukov *et al.*, “Exponential ionic drift: fast switching and low volatility of thin-film memristors,” *Appl. Phys. A*, vol. 94, no. 3, pp. 515–519, Mar. 2009. doi: 10.1007/s00339-008-4975-3
[29] Y. Li *et al.*, “In situ Parallel Training of Analog Neural Network Using Electrochemical Random-Access Memory,” *Front. Neurosci.*, vol. 15, p. 636127, Apr. 2021. doi: 10.3389/fnins.2021.636127
[30] J. Lee *et al.*, “Improvement of Synaptic Properties in Oxygen-Based Synaptic Transistors Due to the Accelerated Ion Migration in Sub-Stoichiometric Channels,” *Adv Elect Materials*, vol. 7, no. 8, p. 2100219, Aug. 2021. doi: 10.1002/aelm.202100219
[31] P. Chen *et al.*, “Open-loop analog programmable electrochemical memory array,” *Nat Commun*, vol. 14, no. 1, p. 6184, Oct. 2023. doi: 10.1038/s41467-023-41958-4
[32] W. Wang *et al.*, “Neuromorphic Motion Detection and Orientation Selectivity by Volatile Resistive Switching Memories,” *Advanced Intelligent Systems*, vol. 3, no. 4, p. 2000224, Apr. 2021. doi: 10.1002/aisy.202000224